

Digital rock physics applied to squirt flow

Simón Lissa¹, Matthias Ruf², Holger Steeb³, and Beatriz Quintal¹

ABSTRACT

We have developed a workflow for computing the seismic-wave moduli dispersion and attenuation due to squirt flow in a numerical model derived from a micro X-ray computed tomography image of cracked (through thermal treatment) Carrara marble sample. To generate the numerical model, the image is processed, segmented, and meshed. The finite-element method is adopted to solve the linearized, quasistatic Navier-Stokes equations describing laminar flow of a compressible viscous fluid inside the cracks coupled with the quasistatic Lamé-Navier equations for the solid phase. We compute the effective P- and S-wave moduli in the three Cartesian directions for a model in dry conditions (saturated with air) and for a smaller model fully saturated with glycerin and having either drained or undrained boundary conditions. For the model saturated with glycerin, the results indicate significant and frequency-dependent P- and S-wave attenuation and the corresponding dispersion caused by squirt flow. Squirt flow occurs in response to fluid pressure gradients induced in the cracks by the imposed deformations. Our digital rock-physics workflow can be used to interpret laboratory measurements of attenuation using images of the rock sample.

INTRODUCTION

The characterization of fluid-saturated rocks plays a fundamental role in several activities such as monitoring of CO₂ geologic sequestration, geothermal energy production, exploration, and production of oil and gas (Klimentos, 1995; Metz et al., 2005; Tester et al., 2007). Seismic waves are known to be affected by rock heterogeneities as well as by the fluid in the pore space; therefore, seismic

methods are important tools for inferring rock and fluid properties. At the microscale, pores and cracks are examples of rock heterogeneities. In fluid-saturated rocks, and considering seismic wavelengths much bigger than the pore sizes, a physical phenomenon known as squirt flow results in seismic attenuation and velocity dispersion (O'Connell and Budiansky, 1977; Murphy et al., 1986). In this process, the deformation of compliant flat pores (pores having a low aspect ratio, such as cracks and grain contacts) produced by a passing seismic wave, creates a fluid pressure gradient between the deformed pore and another stiffer pore if they are hydraulically connected. Then, during fluid pressure diffusion, friction within the viscous fluid dissipates energy. The frequency-dependent seismic response of squirt flow has been studied analytically (O'Connell and Budiansky, 1977; Mavko and Jizba, 1991; Dvorkin et al., 1995; Gurevich et al., 2010), numerically (Quintal et al., 2016, 2019; Das et al., 2019; Alkhimenkov et al., 2020a, 2020b; Lissa et al., 2020), and experimentally (Pimienta et al., 2015a, 2015b; Subramaniyan et al., 2015; Borgomano et al., 2019; Chapman et al., 2019).

Digital rock-physics (DRP) studies aim to numerically reproduce laboratory measurements of rock properties based on high-resolution rock images. Examples of rock properties obtained through DRP are pore-space geometry (Arns et al., 2005; Golab et al., 2010), hydraulic permeability (Fredrich et al., 1993; Sain et al., 2014), electrical conductivity (Arns et al., 2001), and elastic rock moduli (Arns et al., 2002; Saenger et al., 2011; Madonna et al., 2012; Saxena and Mavko, 2016), among others (e.g., Sommacal et al., 2016). Considering that those properties can be obtained on the same sample, one of the most important advantages of DRP is its potential for finding relations between the obtained properties. DRP also provides a detailed insight into the studied physics at the pore scale and can be used as a feasibility analysis for planning laboratory experiments. However, the method has limitations, such as the lack of software and hardware capabilities for considering big enough models, the limited resolution in imaging, and

Manuscript received by the Editor 29 September 2020; revised manuscript received 8 January 2021; published ahead of production 9 April 2021; published online 13 July 2021.

¹University of Lausanne, Institute of Earth Sciences, Lausanne 1015, Switzerland. E-mail: simon.lissa@unil.ch (corresponding author); beatriz.quintal@unil.ch.

²University of Stuttgart, Institute of Applied Mechanics (CE), Stuttgart 70569, Germany. E-mail: matthias.ruf@mechbau.uni-stuttgart.de.

³University of Stuttgart, Institute of Applied Mechanics (CE), Stuttgart 70569, Germany and University of Stuttgart, SC SimTech, Stuttgart 70569, Germany. E-mail: holger.steeb@mechbau.uni-stuttgart.de.

© 2021 Society of Exploration Geophysicists. All rights reserved.

errors in the segmentation processes. These constraints commonly result in differences between laboratory measurements and numerical estimations (Dvorkin et al., 2011; Andrä et al., 2013a, 2013b). As an example, Sarout et al. (2017) invert the geometric crack properties (crack density, aspect ratio, and aperture) of a thermally treated Carrara marble sample from the elastic moduli measured in the laboratory. The inferred crack parameters were significantly lower (one order of magnitude for crack aperture and aspect ratio) than those obtained from segmented 2D microscope images or 3D micro X-ray computed tomography (μ XRCT) images of the same rock sample by Delle Piane et al. (2015). The cause of this difference was attributed to the imaging technique, which is not capable of resolving the smallest heterogeneities of the rock, such as the roughness of crack walls. These limitations represent a fundamental challenge for obtaining accurate DRP results.

A well-known representation of a pore geometry in which squirt flow takes place is a compliant, or low-aspect-ratio, pore that is hydraulically connected to an isometric pore (Murphy et al., 1986; Gurevich et al., 2010). Another classic pore geometry in which squirt flow takes place is interconnected cracks (e.g., O'Connell and Budiansky, 1977). In this scenario, given the orientation of two interconnected cracks, one of them will be more deformed by the passing wave due to its orientation and this will induce a fluid pressure gradient between cracks and thus dissipation.

Recently, Das et al. (2019) present a DRP analysis of a squirt flow scenario. They use the finite-element method to study the fluid dynamics at the pore scale accounting for inertial effects and fluid pressure diffusion. They apply their workflow to a 3D model derived from a μ XRCT image of Berea sandstone and show fluid pressure gradients in the pore space. However, all of the pores present in their model have relatively large aspect ratios; consequently, they observe negligible P-wave modulus dispersion and attenuation due to squirt flow. Quantitative DRP analysis of energy dissipation due to squirt flow remains elusive and in need of further development.

In this work, we present a novel and detailed workflow for numerically obtaining seismic wave moduli dispersion and attenuation caused by squirt flow on models derived from a μ XRCT image of a rock sample having interconnected cracks. For this, a sample of Carrara marble is thermally treated, which initiates cracks at the grain boundaries as a consequence of the anisotropic thermal expansion of the grains; subsequently, a μ XRCT image of the sample is obtained (Ruf and Steeb, 2020a). Filtering, segmentation, and meshing procedures are applied on a subvolume of the rock image to create the 3D numerical model. We provide a detailed description of the model generation workflow. We then solve the coupled Lamé-Navier and Navier-Stokes equations in the solid and the fluid domains, in the frequency domain, neglecting inertia terms and using the finite-element method (Quintal et al., 2019). This numerical solution is based on an upscaling procedure in which the heterogeneous medium behaves as an effective homogeneous viscoelastic medium (Jänicke et al., 2015), which allows us to obtain the P- and S-wave moduli dispersion and attenuation. First, we consider the model in dry conditions to analyze the model size effects on the P- and S-wave velocities by comparing results from the full model with results obtained from a subvolume. The same subvolume is then analyzed under full saturation with glycerin to compute attenuation and dispersion considering drained and undrained boundary conditions. A visualization of the fluid pressure and energy dissipation

rate in the cracks allow for a better understanding of the squirt-flow process.

WORKFLOW

Sample preparation and imaging

In this study, we focus on the attenuation and dispersion of seismic wave moduli due to squirt flow occurring between hydraulically connected cracks. The first step of the work consists of creating a homogeneous, hydraulically connected crack network in an almost nonporous Carrara marble sample. Carrara marble is composed almost entirely of calcite and was proven to be a very suitable material for this purpose; see, for example, Peacock et al. (1994), Delle Piane et al. (2015), and Sarout et al. (2017) because it combines several positive aspects such as a high mineral purity, very low porosity, and permeability.

From a Carrara marble block with thickness of 80 mm, a cylindrical core with a diameter of 30 mm and a length of 80 mm is extracted by using a water-cooled diamond drill. Afterward, we apply a thermal treatment to artificially create the required crack network, which is an often applied method in experimental rock physics (Brotons et al., 2014; Delle Piane et al., 2015; Sarout et al., 2017; Pimienta et al., 2019). For this, the sample is heated up with a heating rate of 3 K/min from room temperature (20°C) to 600°C. We use 600°C as maximum temperature to achieve a maximum effect regarding the initiated crack network volume, but avoiding the calcite decomposition, which significantly starts above 600°C (Rodríguez-Navarro et al., 2009). The heating rate is a compromise between the needed time for the heating-up period and preventing high temperature gradients inside the sample. To ensure a uniform temperature distribution within the sample, the maximum temperature is held for 2 h as shown in Sarout et al. (2017). Then, the sample is slowly cooled down to room temperature, which is performed inside the turned off but still closed furnace, which does not allow a direct control of the cooling rate. The resulting maximum cooling rate is approximately 6.1 K/min and directly occurs after the switching off. With the help of this treatment, cracks are formed at the grain boundaries as a consequence of the anisotropic thermal expansion of the calcite grains during the heating-up phase (Clarke, 1980; Evans and Clarke, 1980; Fredrich and Fong Wong, 1986), which is in general also responsible for the physical weathering of marbles (Siegesmund et al., 2000). Because the thermal anisotropic expansion of the grains depends on the temperature, the applied maximum temperature can be used to influence the initiated crack network volume as experimentally shown, for instance, by Pimienta et al. (2019).

For measuring the bulk volume change, a perfect cylindrical shape of the sample was assumed and the sample's length and diameter were measured before and after the thermal treatment with a micrometer caliper with precision of 0.001 mm. The applied thermal treatment leads to a bulk volume increase of approximately 2.05% under ambient conditions as a consequence of the created crack network volume.

Because we are interested in very small features, it is essential to extract a small sample for the μ XRCT imaging from the thermally treated sample. In our case, a cylindrical core with a diameter of 5 mm and a length of approximately 10 mm is extracted by again using a water-cooled diamond drill. An illustration of the μ XRCT data set is shown in Figure 1. To better show the homogeneous dis-

tribution of cracks, a partial volume is removed. It is possible to observe the initiated crack network (pore space), mainly located at the grain contacts, in dark gray, and the calcite grains in lighter gray. The imaging process results in a voxel size of 2 μm . Further details regarding this process can be found in Appendix A.

Image denoising and segmentation

Considering that applying our workflow to the whole image volume depicted in Figure 1 is computationally very costly, we only analyze two subvolumes. Figure 2 shows a quarter of one slice of the raw μXRCT data set. The orange box pictures the location of the big volume considered in our analysis, which is defined by $x = [1858, 2158]$, $y = [1620, 1920]$, and $z = [135, 435]$ of the open-access images provided by Ruf and Steeb (2020a). The location of the small model is shown by the green box defined by $x = [1858, 2008]$, $y = [1620, 1770]$, and $z = [135, 285]$. The cubes have 150^3 and 300^3 voxels (or 300 and 600 μm side), respectively. For image processing, segmentation, and surface meshing, we use AVIZO 2019.1.

Image denoising

A subvolume of the raw μXRCT image is imported. The *nonlocal means* filter (Buades et al., 2005; Gastal and Oliveira, 2012), which is included in the *sandbox filter*, is used for denoising. The filter works assigning a weight to each voxel based on the similarity of its gray value and the neighborhood voxels inside certain window. A voxel having neighbor voxels with gray values similar to its own gray value receives a high weight. Then, a weighted average is

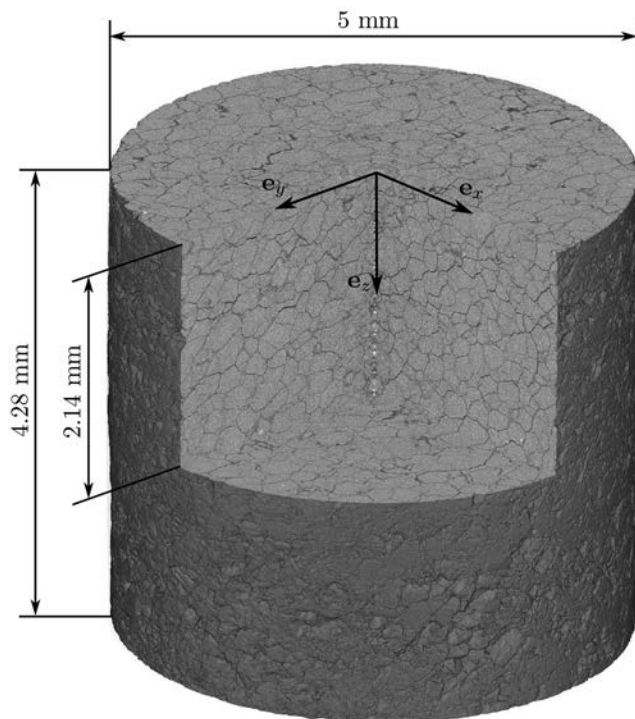


Figure 1. Illustration of the resulting μXRCT data set of the thermally treated Carrara marble core sample with microcracks along the grain boundaries (Ruf and Steeb, 2020a) and definition of the underlying voxel coordinate system used here.

computed for assigning a new gray intensity value to each voxel. The application of this filter increases the contrast between the grain and the cracks, simplifying the subsequent image segmentation. The filter parameters used are a 10-pixel disk-shape search windows in the xy -plane with a local neighborhood of 1.0, and a similarity value of 0.8. The result of its implementation can be observed in Figure 3 in comparison with the raw image for one slice of the cube. Most of the dark-gray values located on the grains have been assigned with lighter gray values, whereas the dark-gray values located on the cracks remain intact. Figure 4 shows the normalized histograms of the raw and filtered images. It is possible to observe an increase in the number of voxels having light-gray values corresponding to the grains (i.e., the histogram peak), as well as a decrease in the number of voxels having dark-gray values.

Segmentation

Using the histograms of the images, an initial selection of the grain phase is manually made. That is the gray intensity values in the range of [0.4-1.0] in Figure 4, which includes the histogram peak. As a result, almost all grains and a significant part of the cracks are selected. Then, to identify the cracks by separating the grains, the *separate objects* module is used. This module creates a map of distances from the inner part of each grain as input to a watershed algorithm (e.g., Beucher and Meyer, 1993; Ohser and Schloditz, 2009). The voxels located at the maximum distances from the inner part of the grains are removed from the grain phase and assigned with a new phase constituting the cracks. The outcome is a suspension, given that there are no contact areas between grains anymore. For fixing this, we delete from the crack phase (and assign to the grain phase) the parts of the cracks having the lightest gray values of the image histogram. Those parts are all the voxels with a gray intensity value located on the right of the red dotted line shown in Figure 4. After this, we obtain a segmentation of two phases

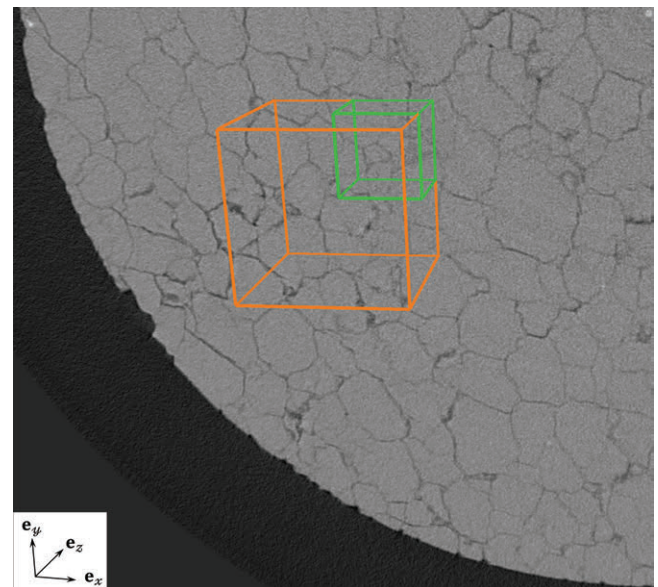


Figure 2. A quarter of the slice 135.tif of the thermally treated Carrara marble μXRCT data set (Ruf and Steeb, 2020a). The cubes show locations of the subvolumes considered in our analysis having 300 μm side (the green cube) and 600 μm side (the orange cube).

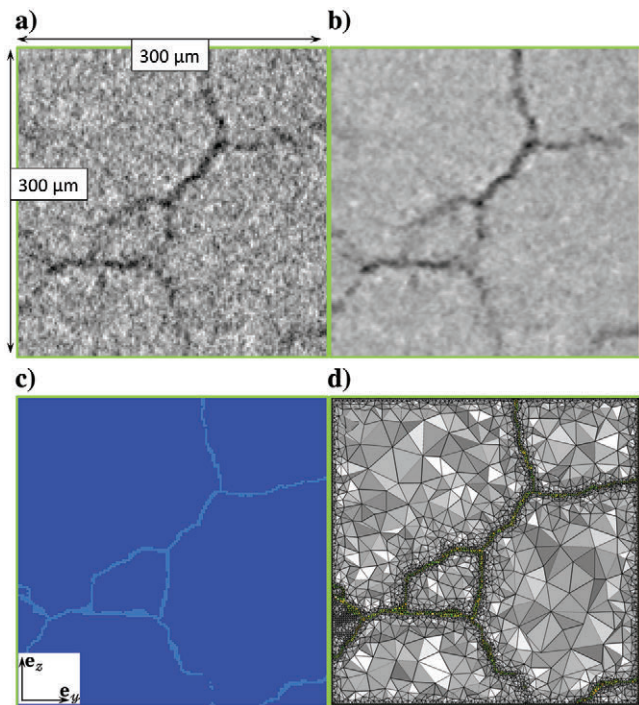


Figure 3. Cross section (yz -plane) for $x = 1974$ of the small sub-volume used in our analysis showing the image processing steps. (a) Raw, (b) filtered, (c) segmented, and (d) meshed.

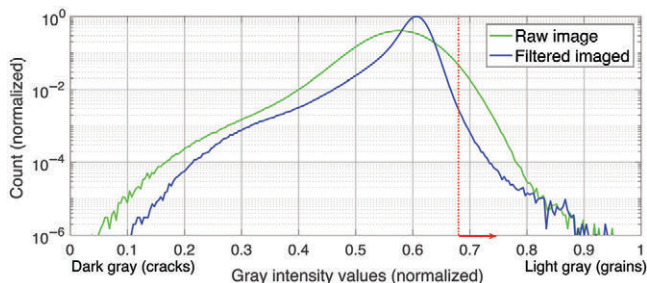


Figure 4. Histograms of the gray intensity values of the raw (green) and filtered (blue) images. The dotted red line corresponds to the selected cutoff (selecting the voxels having gray intensity values in the red arrow direction) to create contact areas between grains during the segmentation process.

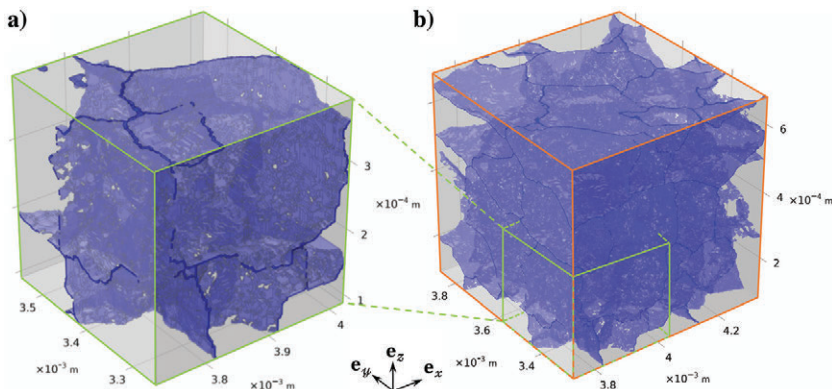


Figure 5. Cubes derived from the μ XRCT images with dimensions of (a) $300\ \mu\text{m}$ side and (b) $600\ \mu\text{m}$ side showing the two segmented phases: the pore space (blue) and the solid grain (transparent gray).

(cracks and grains) having thin cracks and contact areas between grains. At this stage, it is possible to find a small number of voxels corresponding to one phase completely surrounded by voxels corresponding to the other phase. These isolated small number of voxels, or islands, would have negligible effects on the analyzed physics and would still require an important number of mesh elements. For reducing the required mesh elements of the numerical models, we segment as grains all the isolated pore space and as pores all the isolated grains whose volume is lower than 50 voxels (or $400\ \mu\text{m}^3$ approximately) by using the module *remove islands*. Figure 3 shows one slice of the segmented cube. Figure 5 shows the segmented cubes that are formed only by the elastic solid grains (transparent gray) and the pore space (blue). The latest corresponds to the cracks initiated along the grain boundaries.

Meshing the numerical models

After the segmentation process, each segmented cube is converted into a surface format in AVIZO using the *generate surface* module. This module creates triangular elements on every surface between the two segmented phases and on the boundaries of the cubes. The total number of triangular elements constituting the surfaces is 0.9 million for the small model. In the case of the big model, we implement the *remesh surface* module for reducing the number of triangles (by increasing their sizes) from 6 to 1.8 million. The model surfaces are exported as **.stl* files. Note that, at this stage, we have only the grain phase and cube boundaries meshed with triangular elements.

We import the **.stl* files in COMSOL Multiphysics version 5.5 directly into the *mesh* tab. The *detect boundaries* option is used, using a minimum angle of 30° and keeping the default option for the remaining parameters. This criterium properly imports the smallest element of the surface mesh and avoids the intersection between elements that can be created using the minimal elements importing option. Then, the *create domains* module is applied before to create a free tetrahedral volumetric mesh. It assigns a domain number to each closed surface. Given that for our model the grains are fully connected, as well as the cracks, the number of domains is two. The big model cannot be analyzed under glycerin saturation conditions due to computational limitations and the *extremely coarse* size for the tetrahedral elements is selected for the crack and grain domains. Considering the attenuation mechanism intended to be studied in our work, the energy dissipation takes place inside the cracks. Therefore, the *extremely fine* size for the mesh is selected

inside the cracks for the small model, which will be analyzed under glycerin saturation. For reducing the number of elements of the mesh, the *extremely coarse* size of the tetrahedral elements is selected for the grains. Figure 6 shows the mesh for the small model colored by the skewness quality property, which is a measure of the skew of the mesh element angles with respect to the ones of an ideal element. The total number of elements is approximately 4.5 million for the small model and 6.3 million for the big model. Quadratic shape functions are used, and approximately 18 and 26 million degrees of freedom are solved for the small and big models, respectively.

Numerical solution

We use the linearized, quasistatic Navier-Stokes equations to describe the laminar flow of a compressible viscous fluid inside the cracks and pores, coupled with the quasistatic Lamé-Navier equations, for a linear elastic solid (Quintal et al., 2016, 2019). The equations are solved in the frequency domain, and the mathematical formulation is described in Appendix B.

To emulate the deformation caused by either a P- or S-wave in any direction, we apply an harmonic displacement perpendicular (for a P-wave) or parallel (for a S-wave) to one boundary of the model. In addition, we consider either drained or undrained boundary conditions, as the pore space is completely filled with a fluid (air or glycerin). For instance, for the P-wave in the z -direction under drained conditions, no displacements in the x - and y -direction are allowed on the grains at the lateral boundaries (i.e., no constraints on the cracks allowing fluid flow at the boundaries) and no displacements in any direction are allowed at the bottom boundary (i.e., the boundary opposite to that where a perpendicular displacement is applied). To obtain the undrained response we apply the same conditions, but to both grains and cracks on the lateral boundaries. In the case of the S-wave shearing the plane xz under drained conditions, the displacements in the y -direction are set to zero on the grains at the lateral boundaries and the displacements in all directions are set to zero at the bottom (opposite side). To obtain the undrained response on the lateral boundaries too, we wrap the model with a thin layer ($2 \mu\text{m}$) of a solid elastic material with properties $K = 10 \text{ GPa}$ and $\mu = 10 \text{ GPa}$.

After the numerical simulations, we can calculate the effective complex P-wave (H) and S-wave (μ) moduli and the corresponding seismic attenuation (Q^{-1}) as (Lakes, 2009; Jänicke et al., 2015)

$$H_i(\omega) = \frac{\langle \sigma_{ii}(\omega) \rangle}{\langle \epsilon_{ii}(\omega) \rangle}, \quad (1)$$

$$\mu_{ij}(\omega) = \frac{1}{2} \frac{\langle \sigma_{ij}(\omega) \rangle}{\langle \epsilon_{ij}(\omega) \rangle}, \quad (2)$$

$$Q_H^{-1}(\omega) = \frac{\langle \text{Im}[H(\omega)] \rangle}{\langle \text{Re}[H(\omega)] \rangle}, \quad (3)$$

$$Q_\mu^{-1}(\omega) = \frac{\langle \text{Im}[\mu(\omega)] \rangle}{\langle \text{Re}[\mu(\omega)] \rangle}, \quad (4)$$

Table 1. Material properties of the models (Mavko et al., 2009; Pimienta et al., 2016).

Grains (calcite)	Fluid (air)	Fluid (glycerin)
$K^S = 70 \text{ GPa}$	$K^F = 1 \times 10^{-4} \text{ GPa}$	$K^F = 4.35 \text{ GPa}$
$\mu = 30 \text{ GPa}$	$\eta = 2 \times 10^{-5} \text{ Pa} \cdot \text{s}$	$\eta = 1 \text{ Pa} \cdot \text{s}$

Table 2. Velocities of the models in dry conditions.

Velocity	Small model	Big model	Laboratory
V_P^x	4175 m/s	3830 m/s	—
V_P^y	4310 m/s	4170 m/s	—
V_P^z	3700 m/s	2675 m/s	1825 m/s
V_S^{xy}	2420 m/s	2430 m/s	—
V_S^{xz}	2205 m/s	1970 m/s	—
V_S^{yz}	2230 m/s	2005 m/s	1283 m/s

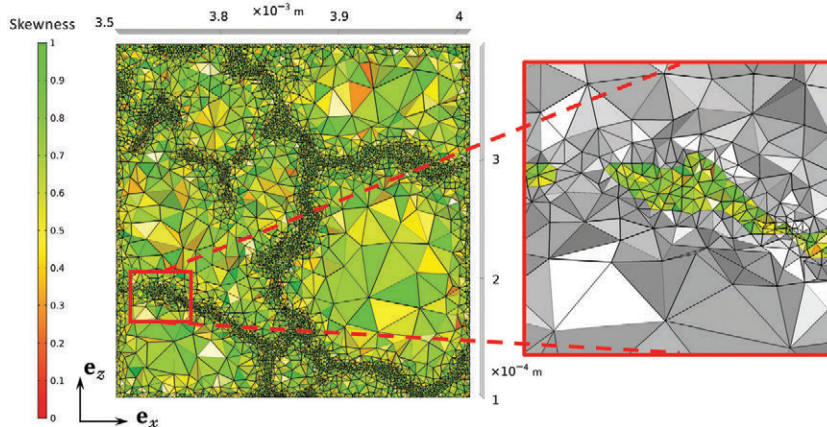


Figure 6. Slice of the small numerical model showing the mesh colored by the quality attribute *skewness*. The inset shows the mesh inside the cracks in colors and the one inside the grains in gray.

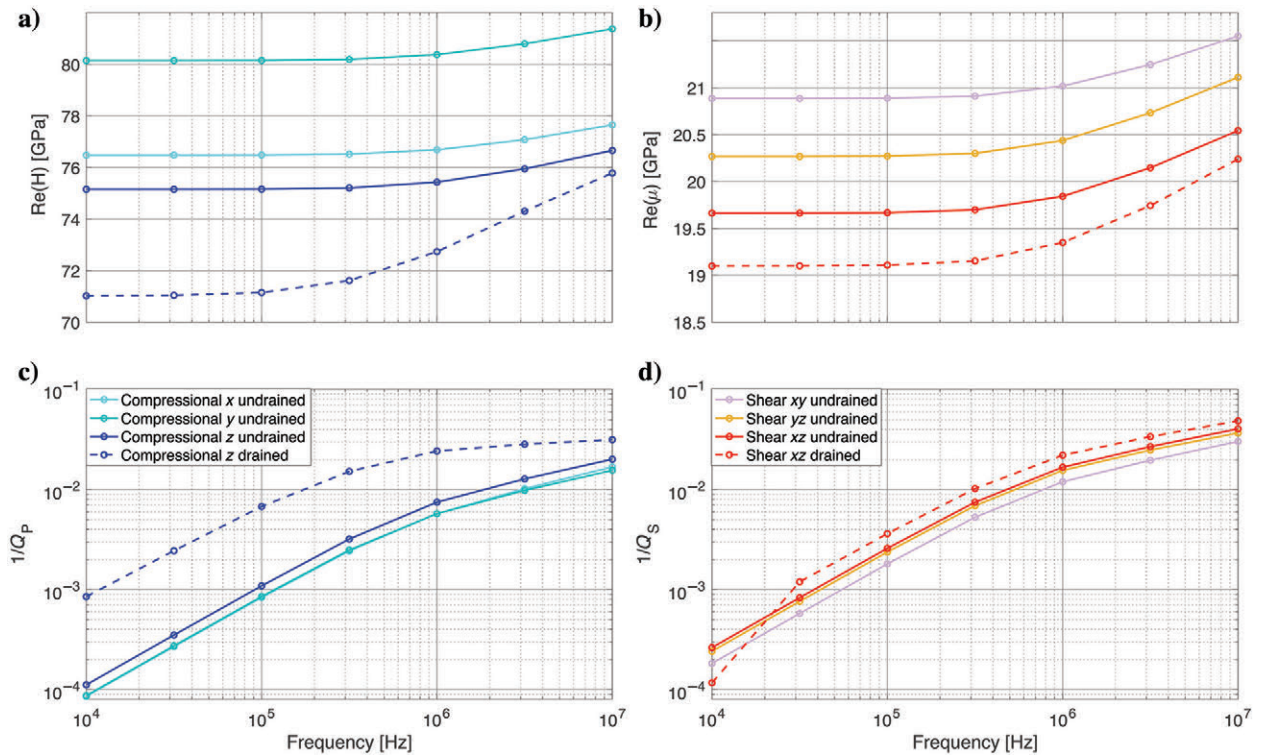
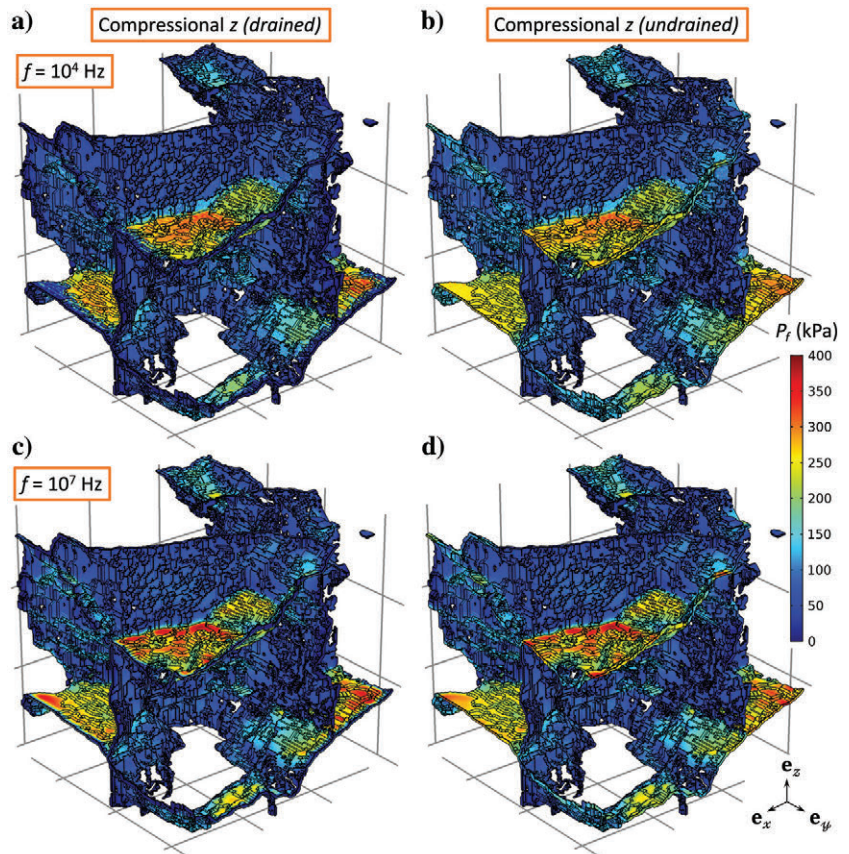


Figure 7. Real part of the (a and b) P- and S-wave moduli, and (c and d) attenuation $1/Q$, in the x-, y-, and z-directions for the small model.

Figure 8. Fluid pressure in the pore space for the whole small model (Figure 5) with (a and c) drained and (b and d) undrained boundary conditions as a response to compressional harmonic tests in the vertical direction with a displacement amplitude of 10^{-3} μm at (a and b) 10^4 Hz and (c and d) 10^7 Hz.



where $\langle \sigma_{ij}(\omega) \rangle$ and $\langle \epsilon_{ij}(\omega) \rangle$ represent the volumetric averages of the stress and strain matrix components σ_{ij} and ϵ_{ij} , respectively, for each angular frequency ω and the Re and Im operators extract the real and imaginary parts of a complex number.

The sizes of the studied numerical models are limited by the hardware used to solve the equations. The simulations are performed for seven frequencies from 10^4 to 10^7 Hz using the direct solver PAR-DISO (Schenk and Gärtner, 2004). For the biggest model considered in this analysis, 800 GB of RAM are used taking 2 h to solve the equations at each frequency.

RESULTS

To analyze the model-size effects on the P- and S-wave velocities, we compare the results from the full model (the big model) with those obtained from a subvolume of it (the small model). The velocities are computed in the three Cartesian directions to analyze potential anisotropic effects and also compared with those obtained from ultrasonic measurements in the laboratory. Then, we analyze the P- and S-wave moduli dispersion and attenuation due to squirt flow for the small model fully saturated with glycerin having either drained or undrained boundary conditions.

Dry conditions

The harmonic numerical test is applied in shear and compressional modes in all three Cartesian directions considering the big and small models presented in Figure 5. We use air properties for the material filling the cracks (Table 1) and a frequency of 10^6 Hz, to be consistent with existing ultrasonic measurements performed on a sibling sample. Considering a grain density of calcite, $\rho_g = 2700 \text{ kg/m}^3$, and a porosity of 4% obtained as the ratio between the volume occupied by the cracks and the volume of the model, we calculate as the weighted average a bulk density for the air-saturated models of $\rho_{\text{bulk}} = 2590 \text{ kg/m}^3$. We compare the numerical results with the ultrasonic P- and S-wave velocities measured on the whole cracked sample (with a diameter of 29 mm and a length 72.5 mm) in dry and unconfined conditions. Table 2 shows these velocities. In general, the numerically obtained velocities exhibit a clear tendency toward lower magnitudes when increasing the model size. Much lower magnitudes can be observed for the velocities measured at the laboratory on the whole sample.

Saturated conditions

To quantify the dissipation taking place in the fluid filling the cracks of the small model, we follow the numerical methodology previously described. Table 1 shows the material properties used for the grain material (calcite) and fluid in the cracks (glycerin), which are assigned to the two phases. The compressibility contrast between the cracks having different orientations and aspect ratios, provided that they are hydraulically connected, induces fluid pressure gradients between them. During the consequent fluid pressure diffusion, friction in the viscous fluid dissipates energy. The real part of the P- and S-wave moduli and the corresponding attenuation in the three Cartesian directions for the small model are presented in Figure 7. At frequencies higher than 10^5 Hz, significant P- and S-wave moduli dispersion and attenuation can be observed. It can also be observed that the maximum attenuation is slightly higher for the S-wave than for the P-wave. This is due to the fact that, such as

during the hemicycle of a wave, the shear test produces a maximum compression on the cracks oriented at 45° from the incidence direction and those oriented at -45° suffer a maximum dilatation. As a result, a higher fluid-pressure gradient is generated compared to that generated by the compressional test that only compresses the cracks. In addition, drained boundary conditions increase the P-wave modulus dispersion and attenuation in the vertical direction for the considered frequency range. In the case of the shear test, drained boundary conditions show results that are more similar to those for undrained boundary conditions.

To better illustrate the squirt flow process, Figure 8 shows the fluid pressure in the pore space with drained and undrained boundary conditions, as a result of the applied compressional harmonic test in the vertical direction with a displacement amplitude of $10^{-3} \mu\text{m}$ at 10^4 and 10^7 Hz. In addition, in Figure 9, a slice of the model shows the fluid pressure in the cracks and the energy dissipation rate (Winter, 1987) at 10^7 Hz calculated as

$$D(\omega) = 2\eta(\dot{\epsilon}_{xx}^2 + \dot{\epsilon}_{yy}^2 + \dot{\epsilon}_{zz}^2 + 2\dot{\epsilon}_{xy}^2 + 2\dot{\epsilon}_{xz}^2 + 2\dot{\epsilon}_{yz}^2) - \frac{2}{3}\eta(\dot{\epsilon}_{xx} + \dot{\epsilon}_{yy} + \dot{\epsilon}_{zz})^2, \quad (5)$$

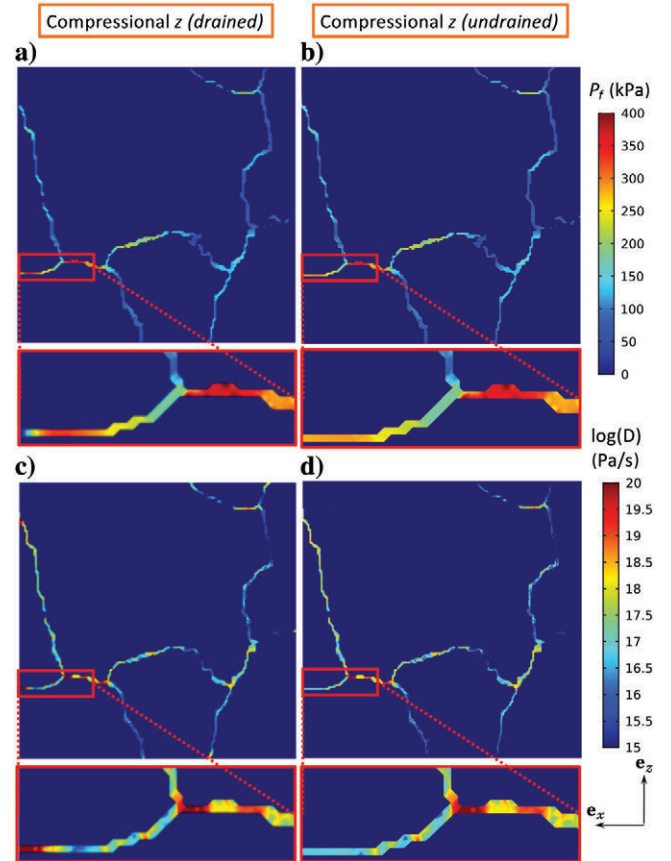


Figure 9. (a and b) Fluid pressure P_f and (c and d) energy dissipation rate D on the plane xz at $y = 3.28 \times 10^{-3} \text{ m}$ for the considered model with (a and c) drained and (b and d) undrained boundary conditions as a response to a compressional harmonic tests in the vertical direction with a displacement amplitude of $10^{-3} \mu\text{m}$ at 10^7 Hz.

DISCUSSION

where a dot on top of a variable implies the multiplication of the variable by $i\omega$. The approximately horizontal cracks exhibit the highest fluid-pressure values (the warm colors), whereas the more vertically oriented cracks are less affected by the deformation in the vertical direction, resulting in lower fluid pressure. The dissipation exhibits maximum magnitudes where the fluid pressure gradients are maximum. In general, the results are similar for both considered boundary conditions except for the cracks located close to the boundaries. When drained boundary conditions are considered, the high fluid pressure in those cracks can partially equilibrate toward the exterior of the model; consequently, stronger dissipation can be observed. Figures 10 and 11 show the fluid pressure in the pore space and the energy dissipation rate for the shear test. It is possible to observe (better in Figure 11) the maximum fluid pressure in the cracks with inclinations close to 45° , whereas cracks with orientations closer to -45° show negative fluid pressure. The fluid pressure diffusion working to equilibrate the pressure gradients between the cracks is responsible for the energy dissipation shown in Figure 7. The dissipation for both considered boundary conditions is similar, which is in agreement with the dispersion and attenuation curves in Figure 7. Overall, both illustrated frequencies in Figures 8 and 10 are lower than the one corresponding to the attenuation peak due to squirt flow; consequently, small differences for the fluid pressure gradients can be observed between them, with the highest pressures occurring at 10^7 Hz.

The numerically calculated velocities for dry conditions (Table 2) tend to be smaller for the big model. However, the velocities for big and small models are similar in comparison with the ones obtained from laboratory measurements, which are much smaller. This significant discrepancy to the laboratory measurements can be explained by the fact that even the big model cannot be considered as an representative element volume (REV), as well as, by the presence of small cracks in the rock that are not recovered by the imaging process. The first argument is also supported by the general reduction of the velocities from the small model to the big model. Moreover, the P-wave velocity in the z -direction (V_p^z) for the big model presents a substantial reduction with respect to the small model. This suggests the predominant presence of horizontal cracks when increasing the model size. In addition, from the volume change of the whole samples after thermal treatment, a 2.05% porosity increment was estimated. In the case of the numerical models, we obtain 3.98% and 4.06% of porosity for the small and big models, respectively. These differences are likely associated with an overestimation of the crack aperture in our segmentation procedure as well as with the fact that the models cannot be considered as an REV.

The results for the fluid-saturated small model show higher attenuation magnitudes for the shear test than for the compressional ones. These observations are in agreement with those obtained by Rubino et al. (2017) for 2D models having orthogonal connected fractures and by Hunziker et al. (2018) for isotropic 2D models having stochastic distributions of fractures represented as poroelastic media, their results for fracture-to-fracture fluid pressure diffusion are analogous to squirt flow in interconnected cracks as shown by Quintal et al. (2016).

The compressional and shear tests on our model exhibit significant attenuation at frequencies higher than 10^6 Hz (Figure 7). From the tendency of the curves, the squirt flow characteristic frequency of the considered model and material properties is expected to occur at frequencies higher than 10^7 Hz at which other attenuation mechanisms could prevail (such as scattering and Biot's global flow). However, as predicted in analytical solutions (e.g., Mavko and Jizba, 1991; Dvorkin et al., 1995; Gurevich et al., 2010), the characteristic frequency is proportional to the cube of the aspect ratio of the compliant cracks. This means that, if the cracks are thinner than the ones segmented in this work, the characteristic frequency would be at lower frequencies. That would be expected for laboratory measurements on the saturated samples given that they must present smaller crack apertures than the ones of our model, which were limited by the underlying maximum spatial resolution of the used μ XRCT system (i.e., the voxel size of $2\ \mu\text{m}$).

For fully saturated porous samples, an attenuation peak associated with the drained-undrained

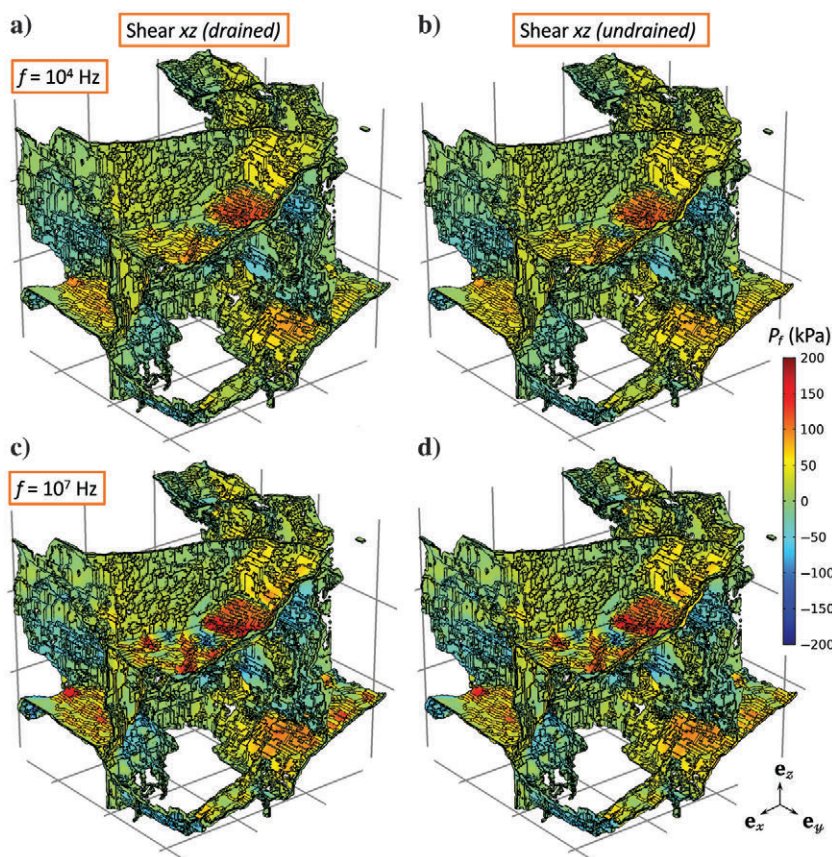


Figure 10. Fluid pressure in the pore space for the whole small model (Figure 5) with (a and c) drained and (b and d) undrained boundary conditions as a response to shear harmonic tests in the plane xz with a displacement amplitude of $10^{-3}\ \mu\text{m}$ at (a and b) 10^4 Hz and (c and d) 10^7 Hz.

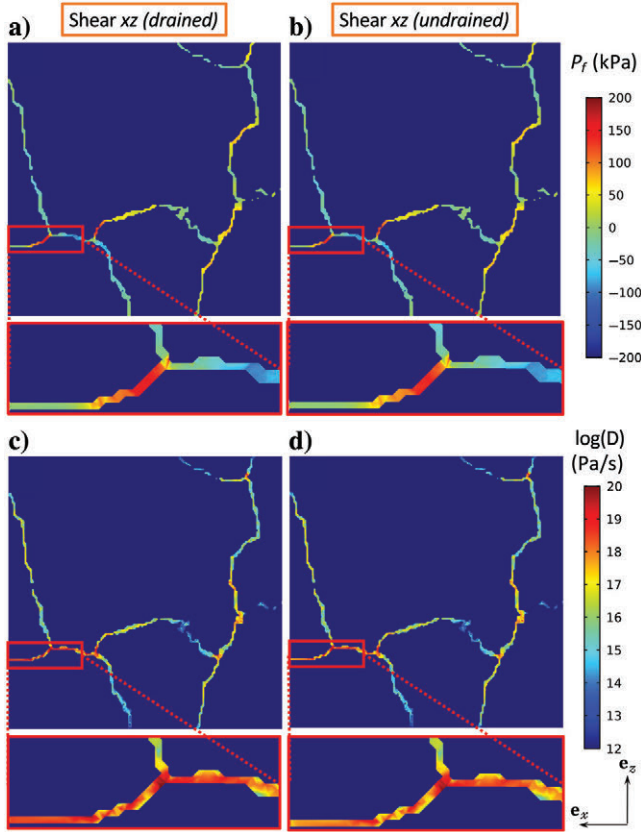


Figure 11. (a and b) Fluid pressure P_f and (c and d) energy dissipation rate D on the plane xz at $y = 3.28 \times 10^{-3}$ m for the considered model with (a and c) drained and (b and d) undrained boundary conditions as a response to a shear harmonic tests in the plane xz with a displacement amplitude of 10^{-3} μm at 10^7 Hz.

transition has been reported in laboratory measurements (e.g., Pimienta et al., 2015b; Chapman et al., 2019). The characteristic frequency associated with the drained-undrained transition is commonly found at significantly lower frequencies than the one corresponding to squirt flow because it is mainly controlled by different properties, such as permeability and sample length, and it occurs at the mesoscopic (sample) scale (Pimienta et al., 2016). The seismic attenuation observed in our study for the models with drained boundary conditions occurs at a similar frequency range than that of the models with undrained boundary conditions because, in both cases, the characteristic frequency is controlled by the crack aspect ratio, leading to an increase in the (squirt) flow process. The attenuation observed for the compressional test was significantly higher for the model with drained boundary conditions due to local fluid pressure diffusion taking place in the cracks close to the model boundaries. In the case of the shear test, minor differences were found between the models with drained and undrained boundary conditions.

CONCLUSION

We presented a complete and detailed workflow for estimating frequency-dependent seismic attenuation and velocity dispersion due to squirt flow based on μXRCT images of rock samples. For that, we first built numerical models by processing and segmenting a subvolume of μXRCT data set, here that of a cracked Carrara mar-

ble sample. We then numerically computed, using the finite-element method, the effective P- and S-wave velocities in all three Cartesian directions for two models of different sizes, the small model being a subvolume of the big one. The models were considered dry, or saturated with air, for these first measurements performed at 10^6 Hz. Although the P-wave velocity in the z -direction shows a considerable discrepancy, presumably due to the preferential presence of horizontal cracks, all the other velocities present a small reduction when increasing eight times the model size. Overall, the model velocities present an approximately isotropic behavior. In addition, the numerically estimated velocities are considerably higher than the ones estimated by laboratory measurements. This is because the numerical models are much smaller than the REV size and the presence of small cracks that are not recovered by the imaging and segmentation processes.

The small model was also analyzed fully saturated with glycerin, considering drained and undrained boundary conditions in a frequency range from 10^4 to 10^7 Hz. Significant P- and S-wave attenuation caused by squirt flow was observed at frequencies greater than 10^6 Hz. Moreover, the S-wave attenuation was higher than the P-wave attenuation. An increase in P-wave attenuation, accompanied by a reduction in the P-wave modulus, was observed when considering drained boundary conditions because these open boundaries also caused squirt flow in the cracks that are directly connected to the boundaries. We found minor differences in the S-wave attenuation when comparing drained and undrained boundary conditions.

ACKNOWLEDGMENTS

We acknowledge support by the Swiss National Science Foundation (grant no. 172691) and the German Research Foundation (grant no. STE 969/13-1). We thank the editors, J. Shragge and E. Liu, and two anonymous reviewers for their helpful comments and suggestions.

DATA AND MATERIALS AVAILABILITY

Data associated with this research are available and can be obtained by contacting the corresponding author. The numerical models (small and big cubes) used for the analysis can be found at: <https://zenodo.org/deposit/4746139#>.

APPENDIX A SAMPLE IMAGING

The scan of the sample is performed in a self-built, modular μXRCT system using an open microfocus tube *FineTec FORE 180.01C TT* with a tungsten transmission target from Finetec Technologies GmbH, Germany, in combination with a *Shad-o-Box 6K HS* detector with a CsI scintillator option from Teledyne DALSA Inc., Waterloo, Ontario, Canada. The latter provides a resolution of 2940×2304 pixels by a pixel pitch of $49.5 \mu\text{m}$. For more details about the system; see Ruf and Steeb (2020b). The geometric magnification is set to 24.78, which leads to the highest achievable spatial resolution of approximately 50 linepairs/mm of the system and results in a voxel size of $2 \mu\text{m}$. With this setting, the corresponding field of view is 5.88 mm in the horizontal direction and 4.61 mm in the vertical direction. Consequently, the sample can be scanned over the entire diameter of 5 mm and basically allows the definition and

extraction of an appropriate REV. The XRCT data set and the related metadata (scan settings) are published (Ruf and Steeb, 2020a).

APPENDIX B

MATHEMATICAL FORMULATION

We use the linearized, quasistatic Navier-Stokes equations, to describe the laminar flow of a compressible viscous fluid inside the cracks and pores, coupled with the quasistatic Lamé-Navier equations, for the linear elastic solid grain (Quintal et al., 2016, 2019). The conservation of momentum is

$$\nabla \cdot \boldsymbol{\sigma} = \mathbf{0}, \quad (\text{B-1})$$

where $\boldsymbol{\sigma}$ is the total stress tensor. In general, each material point can either be occupied by the fluid or the solid phase. Thus, the stress tensor can be written as the sum of the contributions of the solid and the fluid

$$\boldsymbol{\sigma} = \boldsymbol{\sigma}^S + \boldsymbol{\sigma}^F. \quad (\text{B-2})$$

The generalized constitutive equation in the frequency domain is given by

$$\boldsymbol{\sigma} = K^S \text{tr}(\boldsymbol{\epsilon}_S) \mathbf{I} + 2\mu \text{dev}(\boldsymbol{\epsilon}_S) + K^F \text{tr}(\boldsymbol{\epsilon}_F) \mathbf{I} + 2i\omega\eta \text{dev}(\boldsymbol{\epsilon}_F), \quad (\text{B-3})$$

where K^S and μ are the bulk and shear moduli of the solid phase, respectively, K^F and η are the bulk modulus and the shear viscosity of the fluid phase, respectively, $\boldsymbol{\epsilon}_S$ and $\boldsymbol{\epsilon}_F$ are the solid and fluid strain tensors, respectively, tr and dev are the trace and the deviatoric operators, \mathbf{I} is the identity tensor, ω is the angular frequency, and i is the imaginary unit. Acceleration terms are neglected, and squirt flow is the only possible cause for dissipation.

The generalized constitutive equation B-3 is valid for the solid and the fluid domain because it is reduced to Hooke's law in the elastic matrix,

$$\boldsymbol{\sigma}^S = K^S \text{tr}(\boldsymbol{\epsilon}_S) \mathbf{I} + 2\mu \text{dev}(\boldsymbol{\epsilon}_S), \quad (\text{B-4})$$

and inside the cracks is reduced to

$$\boldsymbol{\sigma}^F = K^F \text{tr}(\boldsymbol{\epsilon}_F) \mathbf{I} + 2i\omega\eta \text{dev}(\boldsymbol{\epsilon}_F). \quad (\text{B-5})$$

Combining equations B-1 and B-5 yields the quasistatic, linearized Navier-Stokes equation.

REFERENCES

- Alkhimenkov, Y., E. Caspari, B. Gurevich, N. D. Barbosa, S. Glubokovskikh, J. Hunziker, and B. Quintal, 2020a, Frequency-dependent attenuation and dispersion caused by squirt flow: Three-dimensional numerical study: *Geophysics*, **85**, no. 3, MR129–MR145, doi: [10.1190/geo2019-0519.1](https://doi.org/10.1190/geo2019-0519.1).
- Alkhimenkov, Y., E. Caspari, S. Lissa, and B. Quintal, 2020b, Azimuth-, angle- and frequency-dependent seismic velocities of cracked rocks due to squirt flow: *Solid Earth*, **11**, 855–871, doi: [10.5194/se-11-855-2020](https://doi.org/10.5194/se-11-855-2020).
- Andrä, H., N. Combaret, J. Dvorkin, E. Glatt, J. Han, M. Kabel, Y. Keehm, F. Krzikalla, M. Lee, C. Madonna, M. Marsh, T. Mukerji, E. H. Saenger, R. Sain, N. Saxena, S. Ricker, A. Wiegmann, and X. Zhan, 2013a, Digital rock physics benchmarks — Part 1: Imaging and segmentation: *Computers & Geosciences*, **50**, 25–32, doi: [10.1016/j.cageo.2012.09.005](https://doi.org/10.1016/j.cageo.2012.09.005).
- Andrä, H., N. Combaret, J. Dvorkin, E. Glatt, J. Han, M. Kabel, Y. Keehm, F. Krzikalla, M. Lee, C. Madonna, M. Marsh, T. Mukerji, E. H. Saenger, R. Sain, N. Saxena, S. Ricker, A. Wiegmann, and X. Zhan, 2013b, Digital rock physics benchmarks — Part 2: Computing effective properties: *Computers & Geosciences*, **50**, 33–43, doi: [10.1016/j.cageo.2012.09.008](https://doi.org/10.1016/j.cageo.2012.09.008).
- Arns, C., F. Bauguet, A. Limaye, A. Sakellariou, T. Senden, A. Sheppard, R. Sok, V. Pinczewski, S. Bakke, and L. I. Berge, 2005, Pore scale characterization of carbonates using X-ray microtomography: *SPE Journal*, **10**, 475–484, doi: [10.2118/90368-PA](https://doi.org/10.2118/90368-PA).
- Arns, C. H., M. A. Knackstedt, W. V. Pinczewski, and E. J. Garboczi, 2002, Computation of linear elastic properties from microtomographic images: Methodology and agreement between theory and experiment: *Geophysics*, **67**, 1396–1405, doi: [10.1190/1.1512785](https://doi.org/10.1190/1.1512785).
- Arns, C. H., M. A. Knackstedt, M. V. Pinczewski, and W. B. Lindquist, 2001, Accurate estimation of transport properties from microtomographic images: *Geophysical Research Letters*, **28**, 3361–3364, doi: [10.1029/2001GL012987](https://doi.org/10.1029/2001GL012987).
- Beucher, S., and F. Meyer, 1993, The morphological approach to segmentation: The watershed transformation: *Mathematical Morphology in Image Processing*, **34**, 433–481, doi: [10.1201/9781482277234-12](https://doi.org/10.1201/9781482277234-12).
- Borgomano, J. V. M., L. X. Pimienta, J. Fortin, and Y. Guéguen, 2019, Seismic dispersion and attenuation in fluid-saturated carbonate rocks: Effect of microstructure and pressure: *Journal of Geophysical Research, Solid Earth*, **124**, 12498–12522, doi: [10.1029/2019JB018434](https://doi.org/10.1029/2019JB018434).
- Brotos, V., R. Tomás, S. Ivorra, and A. Grediaga, 2014, Relationship between static and dynamic elastic modulus of calcarenite heated at different temperatures: The San Julián's stone: *Bulletin of Engineering Geology and the Environment*, **73**, 791–799, doi: [10.1007/s10064-014-0583-y](https://doi.org/10.1007/s10064-014-0583-y).
- Buades, A., B. Coll, and J.-M. Morel, 2005, A non-local algorithm for image denoising: *IEEE Computer Society Conference on Computer Vision and Pattern Recognition*, 60–65.
- Chapman, S., J. V. M. Borgomano, H. Yin, J. Fortin, and B. Quintal, 2019, Forced oscillation measurements of seismic wave attenuation and stiffness moduli dispersion in glycerine-saturated Berea sandstone: *Geophysical Prospecting*, **67**, 956–968, doi: [10.1111/1365-2478.12710](https://doi.org/10.1111/1365-2478.12710).
- Clarke, D., 1980, Microfracture in brittle solids resulting from anisotropic shape changes: *Acta Metallurgica*, **28**, 913–924, doi: [10.1016/0001-6160\(80\)90107-8](https://doi.org/10.1016/0001-6160(80)90107-8).
- Das, V., T. Mukerji, and G. Mavko, 2019, Numerical simulation of coupled fluid-solid interaction at the pore scale: A digital rock-physics technology: *Geophysics*, **84**, no. 4, WA71–WA81, doi: [10.1190/geo2018-0488.1](https://doi.org/10.1190/geo2018-0488.1).
- Delle Piane, C., A. Arena, J. Sarout, L. Esteban, and E. Cazes, 2015, Microcrack enhanced permeability in tight rocks: An experimental and microstructural study: *Tectonophysics*, **665**, 149–156, doi: [10.1016/j.tecto.2015.10.001](https://doi.org/10.1016/j.tecto.2015.10.001).
- Dvorkin, J., N. Derzhi, E. Diaz, and Q. Fang, 2011, Relevance of computational rock physics: *Geophysics*, **76**, no. 5, E141–E153, doi: [10.1190/geo2010-0352.1](https://doi.org/10.1190/geo2010-0352.1).
- Dvorkin, J., G. Mavko, and A. Nur, 1995, Squirt flow in fully saturated rocks: *Geophysics*, **60**, 97–107, doi: [10.1190/1.1443767](https://doi.org/10.1190/1.1443767).
- Evans, A. G., and D. R. Clarke, 1980, Residual stresses and microcracking induced by thermal contraction inhomogeneity, in D. P. H. Hasselman and R. A. Heller, eds., *Thermal stresses in severe environments*: Springer US, 629–648, doi: [10.1007/978-1-4613-3156-8_39](https://doi.org/10.1007/978-1-4613-3156-8_39).
- Fredrich, J., K. Greaves, and J. Martin, 1993, Pore geometry and transport properties of fontainebleau sandstone: *International Journal of Rock Mechanics and Mining Sciences Geomechanics Abstracts*, **30**, 691–697, doi: [10.1016/0148-9062\(93\)90007-Z](https://doi.org/10.1016/0148-9062(93)90007-Z).
- Fredrich, J. T., and T. Fong Wong, 1986, Micromechanics of thermally induced cracking in three crustal rocks: *Journal of Geophysical Research, Solid Earth*, **91**, 12743–12764, doi: [10.1029/JB091iB12p12743](https://doi.org/10.1029/JB091iB12p12743).
- Gastal, E., and M. Oliveira, 2012, Adaptive manifolds for real-time high-dimensional filtering: *ACM Transactions on Graphics*, **31**, 1–13, doi: [10.1145/2185520.2185529](https://doi.org/10.1145/2185520.2185529).
- Golab, A., M. Knackstedt, H. Averdunk, T. Senden, A. Butcher, and P. Jaime, 2010, 3D porosity and mineralogy characterization in tight gas sandstones: *The Leading Edge*, **29**, 1476–1483, doi: [10.1190/1.3525363](https://doi.org/10.1190/1.3525363).
- Gurevich, B., D. Makarynska, O. B. de Paula, and M. Pervukhina, 2010, A simple model for squirt-flow dispersion and attenuation in fluid-saturated granular rocks: *Geophysics*, **75**, no. 6, N109–N120, doi: [10.1190/1.3509782](https://doi.org/10.1190/1.3509782).
- Hunziker, J., M. Favino, E. Caspari, B. Quintal, J. G. Rubino, R. Krause, and K. Holliger, 2018, Seismic attenuation and stiffness modulus dispersion in porous rocks containing stochastic fracture networks: *Journal of Geophysical Research, Solid Earth*, **123**, 125–143, doi: [10.1002/2017JB014566](https://doi.org/10.1002/2017JB014566).
- Jänicke, R., B. Quintal, and H. Steeb, 2015, Numerical homogenization of mesoscopic loss in poroelastic media: *European Journal of Mechanics, A, Solids*, **49**, 382–395, doi: [10.1016/j.euromechsol.2014.08.011](https://doi.org/10.1016/j.euromechsol.2014.08.011).
- Klimentos, T., 1995, Attenuation of P- and S-waves as a method of distinguishing gas and condensate from oil and water: *Geophysics*, **60**, 447–458, doi: [10.1190/1.1443782](https://doi.org/10.1190/1.1443782).

- Lakes, R., 2009, *Viscoelastic materials*: Cambridge University Press.
- Lissa, S., N. D. Barbosa, E. Caspari, Y. Alkhimenkov, and B. Quintal, 2020, Squirt flow in cracks with rough walls: *Journal of Geophysical Research, Solid Earth*, **125**, e2019JB019235, doi: [10.1029/2019JB019235](https://doi.org/10.1029/2019JB019235).
- Madonna, C., B. S. Almqvist, and E. H. Saenger, 2012, Digital rock physics: Numerical prediction of pressure-dependent ultrasonic velocities using micro-CT imaging: *Geophysical Journal International*, **189**, 1475–1482, doi: [10.1111/j.1365-246X.2012.05437.x](https://doi.org/10.1111/j.1365-246X.2012.05437.x).
- Mavko, G., and D. Jizba, 1991, Estimating grain-scale fluid effects on velocity dispersion in rocks: *Geophysics*, **56**, 1940–1949, doi: [10.1190/1.1443005](https://doi.org/10.1190/1.1443005).
- Mavko, G., T. Mukerji, and J. Dvorkin, 2009, *The rock physics handbook: Tools for seismic analysis of porous media*: Cambridge University Press.
- Metz, B., O. Davidson, H. de Coninck, M. Loos, and L. Meyer, 2005, IPCC special report on carbon dioxide capture and storage: Cambridge University Press, 431.
- Murphy, W. F., K. W. Winkler, and R. L. Kleinberg, 1986, Acoustic relaxation in sedimentary rocks: Dependence on grain contacts and fluid saturation: *Geophysics*, **51**, 757–766, doi: [10.1190/1.1442128](https://doi.org/10.1190/1.1442128).
- O'Connell, R. J., and B. Budiansky, 1977, Viscoelastic properties of fluid-saturated cracked solids: *Journal of Geophysical Research*, **82**, 5719–5735, doi: [10.1029/JB082i036p05719](https://doi.org/10.1029/JB082i036p05719).
- Ohser, J., and K. Schlätz, 2009, *3D images of materials structures*: John Wiley & Sons Ltd.
- Peacock, S., C. McCann, J. Sothcott, and T. Astin, 1994, Seismic velocities in fractured rocks: An experimental verification of Hudson's theory: *Geophysical Prospecting*, **42**, 27–80, doi: [10.1111/j.1365-2478.1994.tb00193.x](https://doi.org/10.1111/j.1365-2478.1994.tb00193.x).
- Pimienta, L., J. Borgomano, J. Fortin, and Y. Guéguen, 2016, Modelling the drained/undrained transition: Effect of the measuring method and the boundary conditions: *Geophysical Prospecting*, **64**, 1098–1111, doi: [10.1111/1365-2478.12390](https://doi.org/10.1111/1365-2478.12390).
- Pimienta, L., J. Fortin, and Y. Guéguen, 2015a, Bulk modulus dispersion and attenuation in sandstones: *Geophysics*, **80**, no. 2, D111–D127, doi: [10.1190/geo2014-0335.1](https://doi.org/10.1190/geo2014-0335.1).
- Pimienta, L., J. Fortin, and Y. Guéguen, 2015b, Experimental study of Young's modulus dispersion and attenuation in fully saturated sandstones: *Geophysics*, **80**, no. 5, L57–L72, doi: [10.1190/geo2014-0532.1](https://doi.org/10.1190/geo2014-0532.1).
- Pimienta, L., L. F. Orellana, and M. Violay, 2019, Variations in elastic and electrical properties of crustal rocks with varying degree of microfracturation: *Journal of Geophysical Research, Solid Earth*, **124**, 6376–6396, doi: [10.1029/2019JB017339](https://doi.org/10.1029/2019JB017339).
- Quintal, B., E. Caspari, K. Holliger, and H. Steeb, 2019, Numerically quantifying energy loss caused by squirt flow: *Geophysical Prospecting*, **67**, 2196–2212, doi: [10.1111/1365-2478.12832](https://doi.org/10.1111/1365-2478.12832).
- Quintal, B., J. G. Rubino, E. Caspari, and K. Holliger, 2016, A simple hydro-mechanical approach for simulating squirt-type flow: *Geophysics*, **81**, no. 4, D335–D344, doi: [10.1190/geo2015-0383.1](https://doi.org/10.1190/geo2015-0383.1).
- Rodriguez-Navarro, C., E. Ruiz-Agudo, A. Luque, A. B. Rodriguez-Navarro, and M. Ortega-Huertas, 2009, Thermal decomposition of calcite: Mechanisms of formation and textural evolution of CaO nanocrystals: *American Mineralogist*, **94**, 578–593, doi: [10.2138/am.2009.3021](https://doi.org/10.2138/am.2009.3021).
- Rubino, J., E. Caspari, T. Müller, and K. Holliger, 2017, Fracture connectivity can reduce the velocity anisotropy of seismic waves: *Geophysical Journal International*, **210**, 223–227, doi: [10.1093/gji/ggx159](https://doi.org/10.1093/gji/ggx159).
- Ruf, M., and H. Steeb, 2020a, Micro-XRCT data set of Carrara marble with artificially created crack network: Slow cooling down from 600°C, doi: [10.18419/darus-754](https://doi.org/10.18419/darus-754), DaRUS, VI.
- Ruf, M., and H. Steeb, 2020b, An open, modular, and flexible micro X-ray computed tomography system for research: *Review of Scientific Instruments*, **91**, 113102, doi: [10.1063/5.0019541](https://doi.org/10.1063/5.0019541).
- Saenger, E. H., F. Enzmann, Y. Keehm, and H. Steeb, 2011, Digital rock physics: Effect of fluid viscosity on effective elastic properties: *Journal of Applied Geophysics*, **74**, 236–241, doi: [10.1016/j.jappgeo.2011.06.001](https://doi.org/10.1016/j.jappgeo.2011.06.001).
- Sain, R., T. Mukerji, and G. Mavko, 2014, How computational rock-physics tools can be used to simulate geologic processes, understand pore-scale heterogeneity, and refine theoretical models: *The Leading Edge*, **33**, 324–334, doi: [10.1190/tle33030324.1](https://doi.org/10.1190/tle33030324.1).
- Sarout, J., E. Cazes, C. Delle Piane, A. Arena, and L. Esteban, 2017, Stress-dependent permeability and wave dispersion in tight cracked rocks: Experimental validation of simple effective medium models: *Journal of Geophysical Research, Solid Earth*, **122**, 6180–6201, doi: [10.1002/2017JB014147](https://doi.org/10.1002/2017JB014147).
- Saxena, N., and G. Mavko, 2016, Estimating elastic moduli of rocks from thin sections: Digital rock study of 3D properties from 2D images: *Computers & Geosciences*, **88**, 9–21, doi: [10.1016/j.cageo.2015.12.008](https://doi.org/10.1016/j.cageo.2015.12.008).
- Schenk, O., and K. Gärtner, 2004, Solving unsymmetric sparse systems of linear equations with pardiso: *Future Generation Computer Systems*, **20**, 475–487, doi: [10.1016/j.future.2003.07.011](https://doi.org/10.1016/j.future.2003.07.011).
- Siegesmund, S., K. Ullemeyer, T. Weiss, and E. K. Tschegg, 2000, Physical weathering of marbles caused by anisotropic thermal expansion: *International Journal of Earth Sciences*, **89**, 170–182, doi: [10.1007/s005310050324](https://doi.org/10.1007/s005310050324).
- Sommacal, S., A. Fogden, B. Young, W. Noel, A. Arena, L. Salazar, T. Gerwig, Q. Cheng, A. Kingston, D. Marchal, A. M. P. Mazas, C. H. Naides, G. Kohler, and M. Cagnolatti, 2016, 3D multiscale imaging of the distribution of pores, organic matter and oil in place in Vaca Muerta shale samples: SPE/AAPG/SEG Unconventional Resources Technology Conference, 2564–2579.
- Subramaniyan, S., B. Quintal, C. Madonna, and E. H. Saenger, 2015, Laboratory-based seismic attenuation in fontainebleau sandstone: Evidence of squirt flow: *Journal of Geophysical Research, Solid Earth*, **120**, 7526–7535, doi: [10.1002/2015JB012290](https://doi.org/10.1002/2015JB012290).
- Tester, J. W., B. J. Anderson, A. S. Batchelor, D. D. Blackwell, R. DiPippo, E. M. Drake, J. Garnish, B. Livesay, M. C. Moore, K. Nichols, S. Petty, M. Nafi Toksoz, R. W. Veatch, R. Baria, C. Augustine, E. Murphy, P. Negraru, and M. Richards, 2007, Impact of enhanced geothermal systems on us energy supply in the twenty-first century: *Philosophical Transactions of the Royal Society A: Mathematical, Physical and Engineering Sciences*, **365**, 1057–1094, doi: [10.1098/rsta.2006.1964](https://doi.org/10.1098/rsta.2006.1964).
- Winter, H. H., 1987, Viscous dissipation term in energy equations, in J. R. Gordon, ed., *Calculation and measurement techniques for momentum, energy and mass transfer*: American Institute of Chemical Engineers, **7**, 27–34.

Biographies and photographs of the authors are not available.